RESEARCH ARTICLE

NANO · MICRO small
www.small-journal.com

Exploration of Amorphous V_2O_5 as Cathode for Magnesium Batteries

*Vijay Choyal, Debsundar Dey, and Gopalakrishnan Sai Gautam**

Development of energy storage technologies that can exhibit higher energy densities, better safety, and lower supply-chain constraints than the current state-of-the-art Li-ion batteries is crucial for our transition into sustainable energy use. In this context, Mg batteries offer a promising pathway to achieve superior volumetric energy densities than Li-ion but require the development of positive electrodes (cathodes) that exhibit high energy densities at a reasonable power performance. Notably, amorphous materials that lack long range order can exhibit "flatter" potential energy surfaces than crystalline frameworks, possibly resulting in faster Mg^{2+} motion. Here, we use a combination of ab initio molecular dynamics (AIMD), and machine learned interatomic potential based calculations is used to explore amorphous-V_2O_5 as a potential cathode for Mg batteries. Using an AIMD-generated dataset, we train and validate moment tensor potentials that can accurately model amorphous-V_2O_5 Importantly, we find a ≈7 (5) orders of magnitude higher Mg^{2+} diffusivity in amorphous-MgV_2O_5 than crystalline-$Mg_xV_2O_5$ (thiospinel-$Mg_xTi_2S_4$), which is directly attributable to the amorphization of the structure, along with a 10-14% drop in the average Mg intercalation voltage. Our work highlights the potential of amorphous-V_2O_5 as a cathode that can exhibit both high energy and power densities, resulting in the practical deployment of Mg batteries.

1. Introduction

Energy storage technologies are essential for driving humanity's transition to a sustainable future, by facilitating electric vehicles, grid-scale storage, and portable electronics.[1–3] While lithium-ion batteries (LIBs) have long dominated the energy storage landscape due to their high energy density, power performance, and long cycle life, LIBs are increasingly approaching their fundamental limitations,[4–6] which include resource scarcity and supply-chain constraints, safety concerns, and performance degradation over prolonged use.[7] As the demand for more efficient and sustainable energy storage solutions grows, magnesium batteries have emerged as a promising alternative,[8–11] since it enables the use of a metallic anode that results in higher volumetric energy density,[8,12] the lower tendency of Mg metal to form dendrites that enhances safety[13,14] and Mg being a fairly abundant element on the earth's crust that can reduce supply-chain constraints. Despite these advantages, the widespread adoption of Mg batteries is hindered by the poor diffusion of Mg^{2+} in crystalline positive electrode (cathode) materials, especially high energy density oxide chemistries, and the susceptibility to conversion reactions,[15] resulting in poor rate performance and cycle life that limits practical deployment.[11,16–19] Thus, designing new cathodes that can exhibit high energy densities and reasonable power densities is critical for the advancement of Mg batteries, which is the focus of this work.

State-of-the-art (SOTA) Mg batteries utilize low-voltage (and hence low energy density) sulfide cathodes, such as Chevrel-$Mg_xMo_6S_8$[20] and thiospinel-$Mg_xTi_2S_4$,[21] which offer structural stability, reasonable rate performance, and reversible Mg intercalation. In case of oxides, several materials that have shown an ability to intercalate Li^+ have been explored as Mg cathodes in an attempt to improve the energy density of Mg batteries. For example, V_2O_5 is one of the first oxides to be explored as a potential cathode for Mg batteries,[22–26] with experiments often reporting limited Mg intercalation (and hence limited capacity) due to poor kinetics[27] and capacity fade with cycling. Spinel-Mn_2O_4 has been shown to electrochemically intercalate Mg ions at a voltage of ≈2.9 V, but its practical performance is limited by cation inversion in the structure that blocks Mg diffusion pathways.[28] Spinel-Cr_2O_4 offers a higher theoretical voltage (≈3.6 V) and is not as prone to cation inversion compared to Mn_2O_4,[29] but suffers from synthesis bottlenecks and electrolyte instability at high voltages. Mixed transition metal spinel oxides, such as Cr-V and Cr-Mn, have reported limited success in intercalating Mg in the bulk, with capacity fade still an ongoing challenge.[30,31] Theoretical calculations have predicted facile Mg transport in post-spinel oxides,[32] but experimental validation of such predictions are not available so far. Although several studies have reported improved Mg cathode performance with the introduction of water into the electrolyte,[8] with solvent intercalation often attributed to aid in Mg diffusion in such cases,[33,34] the capacity and rate performance improvements with water addition can also be caused by proton

V. Choyal, D. Dey, G. Sai Gautam
Department of Materials Engineering
Indian Institute of Science
Bengaluru, Karnataka 560012, India
E-mail: saigautamg@iisc.ac.in

The ORCID identification number(s) for the author(s) of this article can be found under https://doi.org/10.1002/smll.202505851

DOI: 10.1002/smll.202505851

intercalation.[35] Thus, enhancing the rate performance in oxide-based chemistries, via improvements in Mg mobility in the bulk, is critical in the design of cathodes that can deliver higher energy densities compared to the SOTA Mg cathodes.

One of the reasons attributed for poor Mg diffusion (compared to Li) in oxide lattices is the stronger electrostatics of the Mg^{2+}—O^{2-} bonds (vs Li^{+}—O^{2-}) resulting in the need for larger distortions within the structure as Mg^{2+} migrates within the lattice.[36] In other words, the stable site(s) that Mg sits in a given lattice is often "deep" within the potential energy surface (PES), which in turn creates a large migration barrier (E_a) that Mg^{2+} must cross for macroscopic diffusion. Indeed, the insertion of Mg^{2+} into anatase-TiO_2 has been shown to induce cooperative lattice distortion that deepen the energy of the stable sites that Mg occupies instead of perturbing the transition state's energy during migration, resulting in an increase in E_a from 537 to 1500 meV with Mg insertion.[37] One strategy to reduce E_a, as proposed by Rong et al.,[17] is to use structures where Mg^{2+} occupy "unpreferred" (i.e., non-octahedral) coordination environments, which can increase the energy of the stable sites thereby "flattening" the PES and reducing E_a. While the strategy of Rong et al. has shown limited success, such as the identification of spinel Mg-ionic conductors[38,39] and the use of spinel-oxides as Mg cathodes,[18,28,40,41] the mobility enhancements in oxides remain insufficient to surpass the performance of SOTA Mg cathodes.

Another approach to achieve a flatter PES is to reduce the long range order (LRO) of oxides, via amorphization for example, which can reduce the depth of the stable sites that Mg^{2+} occupy and facilitate Mg mobility. Note that diffusion is known to be significantly faster in the highly defective regions (such as grain boundaries) rather than the perfect crystalline regions of a microstructure, especially in systems where the diffusivity in the bulk is "low" ($\approx 10^{-14}$ cm^2 s^{-1} or below at 300 K), as in the case of metals.[42] In grain boundaries, as with amorphous solids, the LRO of the lattice is disrupted, resulting in an increase in the energy of the "stable" sites that atoms occupy and a flatter PES. Therefore, 3*d* transition metal containing redox-active oxide chemistries that can exhibit an amorphous structure may improve Mg mobility in the "bulk" significantly and can function as potential cathodes in Mg batteries. However, such amorphous structures are likely to be metastable and hence reduce the Mg (de)intercalation voltages. Nevertheless, it is worthwhile to explore if amorphous oxides can be used as possible cathodes for Mg batteries. Given that V_2O_5 has been explored as a cathode before for Mg batteries, in both its bulk orthorhombic and nanocrystalline xerogel forms,[11,26,27,33,34] and the ability of V_2O_5 to become amorphous[43] and intercalate ions,[44,45] we choose V_2O_5 as a possible amorphous oxide cathode for Mg batteries in this work. Notably, a recent study has reported the use of V_2O_5-P_2O_5 composite glass system as a cathode material for Mg batteries.[46]

Modeling amorphous structures computationally is non-trivial, since structural models need to be "large" enough to ensure LRO is broken over sufficiently long distances and the sampling of the ionic dynamics needs to be "long" enough so that the transport properties can be accurately estimated. While density functional theory (DFT) and ab initio molecular dynamics (AIMD) calculations enable accurate predictions of material properties, both techniques have severe limitations on the system sizes (≈a few 100s of atoms) and time scales (≈100 ps) that can be accessed.[47] Notably, machine learned interatomic potentials (MLIPs) that are trained on small-scale DFT/AIMD-generated datasets, can provide both "quick" and "accurate" estimates of energies and atomic forces, enabling classical molecular dynamics (MD) simulations that can sample large length and long time scales.[48–55] Typically, MLIPs learn the influence of different "local" coordination environments on an atom of interest, from the DFT/AIMD-generated dataset, to predict the energy of and the forces on the atom.[56] Here, we choose the moment tensor potential (MTP)[57,58] framework, since its accuracy and computational speed has been showcased in several studies, such as predicting ionic diffusivities in solid electrolytes,[59] modeling ionic transport across interfaces,[60] and describing the PES of multi-component systems.[61] MTP models the local coordination environment (within a cut-off radius) around an atom of interest via contracted moment tensors, which consist of radial distribution functions to describe distances and outer products of position vectors of neighbouring atoms to describe angular interactions.[58] Additionally, MTP incorporates an active learning framework[62] that can be used to validate and refine a pre-trained MTP when employed in larger MD simulations.

In this study, we combine DFT/AIMD and MTP-based MD simulations to explore the utility of amorphous-V_2O_5 as a potential cathode for Mg batteries. To construct the MTP, we generate an AIMD-simulated dataset of V_2O_5 and MgV_2O_5 across different temperatures, using the melt-quench technique, resulting in an overall dataset of 3156 configurations. Upon training the MTP on a train subset and optimizing its hyperparameters on the test subset, we fine-tune and validate the trained MTP using active learning, resulting in a final overall dataset of 3725 configurations. To ensure the amorphous nature of the structures generated using AIMD and MTP-MD, we examine the radial distribution functions (RDFs) and LRO at different temperatures in both V_2O_5 and MgV_2O_5. Subsequently, we quantify the impact of amorphization on Mg intercalation voltages and perform large-scale ($2 \times 4 \times 6$ supercell) and long-time (4 ns) MTP-based MD simulations to quantify Mg transport within amorphous MgV_2O_5. We observe a 10–14% drop in the average Mg intercalation voltage (vs Mg metal) due to amorphization of the V_2O_5 structure. Importantly, we find an increase in Mg diffusivity by ≈7 orders of magnitude in amorphous-MgV_2O_5 compared to crystalline-(Mg)V_2O_5, corresponding to a low effective E_a of 47 meV in the amorphous structure. Moreover, the Mg diffusivity in amorphous-MgV_2O_5 is higher than the SOTA $Mg_xTi_2S_4$ by ≈5 orders of magnitude at 300 K, while maintaining a higher average intercalation voltage than the SOTA. Also, we observe Mg motion to be highly cross-correlated at low temperatures with the motion becoming increasing random with increasing temperature. Thus, our work indicates the impact that amorphization can have on improving the Mg mobility in oxide lattices while ensuring that the energy density remains higher than SOTA sulphide and selenide cathodes. We are hopeful that our work will facilitate the practical deployment of Mg batteries by the design of optimized high-energy-density amorphized oxide cathodes. Finally, our theoretical framework is general and can be used to explore other promising amorphous compositions/structures, for Mg battery applications and beyond.

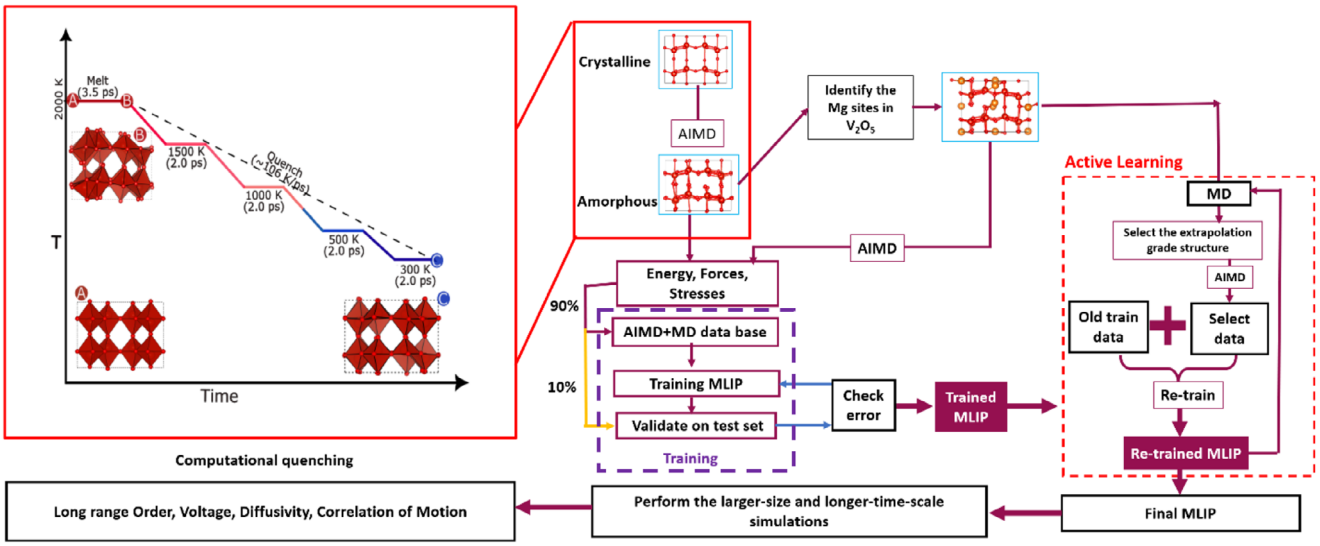

Figure 1. Workflow of dataset generation, DFT calculations, and MLIP training employed in this work. Train and test subsets are used for training and optimizing hyperparameters of the MLIP, respectively. The accuracy of the trained MLIP is validated by using active learning. Voltages and diffusivities are extracted from long-range and large-scale MD simulations performed using the optimized MLIP.

2. Experimental Section

2.1. Workflow

Figure 1 displays the workflow of the study, including data generation and the calculations employed, training of MTP, and active learning to further refine and validate the MTP for the V_2O_5 and MgV_2O_5 systems. After obtaining the initial structure of V_2O_5 from the inorganic crystal structure database (ICSD),[63] melt-quench AIMD simulations were performed to obtain amorphous structures of V_2O_5, which forms the computed dataset of V_2O_5. Subsequently, possible sites that Mg could occupy within the amorphous structures were identified using the TopographyAnalyzer[64] class of pymatgen,[65] and further AIMD calculations were performed to create the MgV_2O_5 dataset. Combining the generated amorphous V_2O_5 and MgV_2O_5 datasets to create the overall dataset, the overall dataset was randomly divided into a 90:10 training:test split, and the training subset was used to construct the MTPs. During training, the hyperparameters of MTP were optimized to minimize the root mean square error (RMSE) and the mean absolute error (MAE) with respect to AIMD-calculated energies and forces on the train and test sets, with the optimized hyperparameters compiled in Table S1 (Supporting Information). Further, the MTPs were tested by performing MD simulations with active learning[62] to refine the training dataset and the validate MTP itself. After ensuring that the hyperparameter-optimized MTPs provided minimal breaks during the active learning step, larger-size and longer-time MD simulations were subsequently performed at different temperatures to obtain Mg intercalation voltages and diffusivities.

2.2. Dataset Generation and MTP Construction

Amorphous V_2O_5 structures were generated via the well-known melt-quench simulation technique[66,67] using AIMD calculations. Specifically, V_2O_5 was heated to a temperature of 2000 K, which was beyond its melting point.[27,68] Subsequently, the molten V_2O_5 was quenched in steps, at an overall cooling rate of 106 K ps^{-1}. During quenching, the V_2O_5 structure was cooled and equilibrated for 2 ps at temperatures of 1500, 1000, and 500 K, before eventually quenching to 300 K. Subsequently, structures were extracted and equilibrated at 1200, 900, and 600 K during the quenching process, to obtain access to amorphous V_2O_5 structures at these intermediate temperatures. The radial distribution functions (RDFs) of V—V, V—O, and O—O bonds and the long range order (LRO) were tracked to verify the amorphous nature of the quenched structure at different temperatures (i.e., 1200, 900, and 600 K). Eventually, the AIMD simulations runs (and active learning) gave rise to 2518 configurations that constituted the V_2O_5 dataset, which was split into 2292 configurations for training and 226 for testing.

In order to generate the dataset of MgV_2O_5, potential sites that Mg can occupy in the amorphous V_2O_5 structure were identified at 300 K, and at each of the three intermediate temperatures, i.e., 1200, 900, and 600 K. The number of possible sites Mg can occupy is typically higher than the stoichiometrically allowed number of occupied Mg sites to maintain a composition of MgV_2O_5. Hence, symmetrically distinct occupations of Mg atoms were enumerated among the possible sites that satisfied the MgV_2O_5 stoichiometry, the different configurations were ranked based on their electrostatic energy (as calculated by the Ewald summation technique[69] and the lowest electrostatic energy structure was chosen for further AIMD simulations. The choice of this workflow is to mimic a typical topotactic insertion process that occurs in intercalation electrodes.[70,71] The final amorphous MgV_2O_5 dataset (including active learning) generated contains 1207 configurations out of which 151 were used for testing. Note that one structure was sampled for every 50 time steps in the AIMD simulations of V_2O_5 and MgV_2O_5 at 300, 600, and 900 K, while one structure was sampled for every 20 time steps in the simulations at 1200 K, since the configurations at 1200 K are typically more disordered compared to the lower temperatures. Combining

the MgV_2O_5 and V_2O_5 datasets, the overall dataset thus contains 3725 configurations, which were split into training (3348) and test (377) subsets.

A detailed description of the MTP framework could be found elsewhere.[58,61] Initially, the training set generated from AIMD calculations was used to train the MTP, and the optimal hyperparameters (Table S1, Supporting Information) were obtained by minimizing errors in the test set. To ensure that the trained potential is good enough for larger-scale MD simulations, active learning,[57,62] was used during MD on a 1 × 2 × 3 supercell to determine if MTP was able to "extrapolate" beyond the training set. Specifically, an extrapolation threshold of 2 was used to determine whether the energy and force predictions on the encountered structures were accurate or not. Once the extrapolation threshold of any encountered structure reached a pre-defined break value of 10, the MD simulation was stopped. Subsequently, the non-accurate structures were calculated with DFT, added to the training set, and the MTP was retrained. Notably, MTP was found to break during active learning only in MD simulations at 1200 K, indicating the highly disordered nature of the structures often encountered at this temperature, while the active learning runs at lower temperatures (900, 600, 300 K) did not break for 4000 ps. A total of 569 structures were generated during active learning that were added to the training dataset (i.e., 569 out of 3348 sampled for the optimized MTP) apart from the original AIMD simulations. Finally, the large-scale and long-time MD simulations were performed without active learning, utilizing the retrained MTP, upon ensuring that the active learning runs on the 1 × 2 × 3 supercell were not broken for 4000 ps at 1200 K.

2.3. DFT and MD Calculations

All the AIMD simulations were done at the DFT-level of theory using the Vienna ab initio simulation package,[72,73] by employing projector-augmented wave potentials.[74] Using a plane-wave kinetic energy cutoff of 520 eV, the Hubbard U corrected strongly constrained and appropriately normed (i.e., SCAN+U) functional was employed to describe the electronic exchange and correlation.[75–78] The U value applied on V d orbitals was 1.0 eV, as derived in previous work.[75,76] The irreducible Brillouin zone was sampled using Γ-centred Monkhorst-Pack[79] k-point meshes with a density of at least 32 per Å (i.e., a minimum of 32 subdivisions along a unit reciprocal space vector), and the Fermi surface was integrated with a Gaussian smearing of width 0.05 eV. No underlying symmetry of any structure was preserved during the calculations. For relaxing the initial V_2O_5 structure, both the total energies and atomic forces were converged to within 0.01 meV and 30 meV $Å^{-1}$, respectively.

AIMD simulations were performed on a 1 × 2 × 3 supercell of V_2O_5 (and MgV_2O_5), corresponding to 84 (96) atoms, with a time step of 2 fs to ensure both accuracy and computational efficiency. Classical MD simulations were performed, also with a time step of 2 fs, based on the constructed MTPs, using the large-scale atomic/molecular massively parallel simulator (LAMMPS)[80] for two different supercell sizes of both V_2O_5 and MgV_2O_5, namely, 1 × 2 × 3 and 2 × 4 × 6. All AIMD and classical MD simulations used an *NVT* ensemble using a Nose-Hoover thermostat[81] and the velocity-Verlet algorithm[82,83] for integrating the equations of motion. For MTP-based MD simulations, the amorphous structures were equilibrated at each temperature using the *NVE* ensemble for 50 ps to randomize the velocities, followed by sampling (to estimate diffusivities) using the *NVT* ensemble for 4 ns. For calculating the intercalation voltage (see below) using MTP at 0 K, a structural relaxation was performed with LAMMPS by applying strict convergence criteria of 10^{-8} eV for the total energy and 10^{-8} eV $Å^{-1}$ for the atomic forces.

For calculating average intercalation voltages, amorphous MgV_2O_5 structures were obtained, after a simulation time of 20 ps at different temperatures, both from AIMD and MTP-based MD, and a single self-consistent field (SCF) calculation with DFT was performed, where the total energies were converged to within 0.01 meV. Subsequently, the Mg atoms were removed from each considered amorphous MgV_2O_5 structure, and a SCF calculation was performed on the corresponding deintercalated V_2O_5 structure, mimicking a topotactic Mg deintercalation process. The SCF calculations on the AIMD/MD structures were performed primarily to ensure that the energy scales are the same, especially with respect to the calculated total energy of Mg metal, which is required to set the reference in the voltage calculations to Mg^{2+}/Mg. Thus, the voltage calculations primarily capture the effect of disorder in the V_2O_5 structure. Given the SCF-calculated energies of MgV_2O_5 ($E_{MgV_2O_5}$) and V_2O_5 ($E_{V_2O_5}$), and the SCAN-calculated total energy of the hexagonal close-packed ground state of Mg metal (E_{Mg}), the average Mg intercalation voltage, versus Mg metal, was approximately calculated as in Equation (1).[84,85] The factor of two in the denominator of Equation (1) corresponds to an exchange of two electrons per Mg^{2+} exchanged, and F is the Faraday's constant.

$$V = -\frac{E_{MgV_2O_5} - E_{V_2O_5} - E_{Mg}}{2F} \tag{1}$$

2.4. Diffusivity Estimations

Ionic motion in solids is often measured using a tracer species with a diffusion coefficient, D^*, which is referred to as the self or tracer diffusivity. In principle, D^* can be computed using a linear fit of the mean-squared displacement (MSD) of moving ions over time (t), as in Equation (2).[86] Note that the MSD in Equation (2) is averaged over all the N hopping ions, while d indicates the dimensionality of the system (typically 3 in solids).

$$D^* = \frac{1}{2d} \lim_{t\to\infty} \frac{1}{N} \sum_{i=1}^{N} \frac{\left|\vec{r}_i(t) - \vec{r}_i(0)\right|^2}{t} \tag{2}$$

In AIMD and MD simulations, the total simulation time (t_{tot}) is often limited due to computational constraints, leading to statistical noise in the extracted MSD. Hence, the total mean squared displacement (TMSD, see Equation 3) that is averaged over multiple time intervals to mitigate statistical fluctuations was used, as proposed by He et al.[86] N_{Δ_t} in Equation (3) represents the number of possible time intervals with duration Δt.

$$\mathrm{TMSD}(\Delta t) = \sum_{i=1}^{N} \frac{1}{N_{\Delta_t}} \sum_{t=0}^{t_{tot}-\Delta t} \left|\vec{r}_i(t+\Delta t) - \vec{r}_i(t)\right|^2 \tag{3}$$

Subsequently, D^* can be calculated as the slope of the MSD over time interval Δt (see Equation 4), where $\text{MSD}(\Delta t) = \frac{\text{TMSD}(\Delta t)}{N}$ and varies linearly with Δt.

$$D^* = \frac{\text{MSD}(\Delta t)}{2d\Delta t} \tag{4}$$

For the MD simulations that were conducted over a total duration of 4000 ps, $\Delta t = 200$ ps was chosen for calculating the MSD and D^*, while for AIMD simulations that lasted for 50 ps, $\Delta t = 10$ ps was chosen.

Note that the TMSD and MSD as defined in Equations (2) and (4) track the displacements of individual ions, while similar TMSD and MSD values can be calculated for the displacement of the centre of mass of the mobile ions – MSCD or mean squared centre-of-mass displacement – with Δt. The slope of MSCD(Δt) versus Δt yields the jump diffusivity (D_J) of the mobile ions, which in turn is related to the chemical diffusivity (D_c), as defined in Fick's first law,[87] by the thermodynamic factor (Θ), as $D_c = \Theta D_J$.[86] The difference between D_J and D^* indicates the extent of cross-correlation among migrating ions in a system, which is often quantified using Haven's ratio (H_R), as $H_R = \frac{D^*}{D_J}$. If a system exhibits completely uncorrelated motion (i.e., purely random motion), then $H_R = 1$, with deviations away from 1 indicating the extent of cross-correlation.

Finally, the diffusivity (D, tracer or jump) can be correlated with E_a that controls the ionic migration via the Arrhenius relation of Equation (5). D_0 is the pre-exponential factor, which includes factors such as jump distance and attempt frequency, k_B is the Boltzmann constant, and T is the temperature. Thus, E_a, which is a material-specific property, can be obtained as the slope of the logarithm of D versus $1/T$. The DiffusionAnalyzer class of pymatgen[88,89] was utilised for post-processing the AIMD and MD calculations, extracting D^* and D_J, and calculating E_a based on D^*.

$$D = D_0 \exp\left(-\frac{E_a}{k_B T}\right) \tag{5}$$

2.5. Statistical Analysis

A total of 3725 atomic configurations of MgV_2O_5 and V_2O_5, generated using ab initio molecular dynamics (AIMD) simulations were used for both training and testing the moment tensor potential (MTP) model. All datapoints were used without any preprocessing. The AIMD energies have a mean and standard deviation of -11.23 ± 0.20 eV, while the MTP energies exhibit -11.22 ± 0.21 eV. In case of atomic forces, the AIMD values were -1.34 ± 9.40 eV Å^{-1}, and the predicted values were -1.00 ± 9.49 eV Å^{-1}. Software packages used for data analysis included python (version 3.12), and Microsoft Excel.

3. Results

3.1. Optimized MTP for MgV_2O_5 and V_2O_5

The parity plots between the final, optimized MTP and AIMD calculated energies and forces, in both the training and test sets are shown in Figure S1 (Supporting Information). Importantly, the constructed MTP demonstrates promising accuracy on the training data. For the energies, the RMSE and MAE are 4.68 and 2.97 meV atom^{-1}, respectively, and for the atomic forces, the RMSE and MAE are 0.243 and 0.113 eV Å^{-1}, respectively, on the training set. The corresponding values on the test set are similarly accurate, with an RMSE and MAE of 3.16 and 2.33 meV atom^{-1} for energies, and 0.244 and 0.116 eV Å^{-1} for forces. In terms of stress predictions, the optimized MTP yields an RMSE of 0.65 GPa and MAE of 0.17 GPa on the training set, and an RMSE of 0.50 GPa and MAE of 0.15 GPa on the test set. To further verify the accuracy of our constructed MTP, we also examined the potential energy landscapes generated by MTP during MD and compared that with AIMD generated data across different temperatures (see Figure S2, Supporting Information). For example, we observe a high degree of overlap between the potential energies calculated by MTP-based MD with AIMD values, beyond simulation times of 1 ps, for both V_2O_5 and MgV_2O_5 at the different temperatures considered, indicating the high degree of accuracy we can obtain with MTP-based MD. Thus, we believe that our optimized potential has the ability to describe the dynamics of both V_2O_5 and MgV_2O_5 systems with a high degree of accuracy.

3.2. RDFs and LRO

We examine the RDFs and LRO of the generated V_2O_5 and MgV_2O_5 structures to verify their amorphous nature upon melt-quench simulations. **Figure 2** presents the RDFs for V_2O_5 (panels a, b, and c) and MgV_2O_5 (d, e, and f), at select temperatures and calculated by both AIMD and MTP. The calculated RDFs at other temperatures are compiled in Figures S3–S5 (Supporting Information). For example, Figure 2a displays the RDFs of the O—O (blue), V—V (red), and V—O (green) bonds in pristine V_2O_5, upon DFT relaxation at 0 K. Thus, Figure 2a represents the RDF in crystalline V_2O_5, which is characterized by sharp peaks for all types of bonds, and serves as a reference for comparing RDFs generated at other temperatures. Figure 2b shows the RDF in the AIMD generated V_2O_5 at 2000 K, after 4 ps of simulation time. In comparison to 0 K, the RDFs of all bonds show less-intense and broader peaks, with no discernable peaks beyond a distance of 6 Å, highlighting the significantly disordered state of V_2O_5 at 2000 K. Importantly, even at a high degree of disorder, the V—O RDF peak at ≈2 Å is dominant, indicating that several of the V—O bonds that form the VO_6 octahedra or VO_5 square pyramids in crystalline-V_2O_5 are intact. The fact that V—O bonds are intact implies that the disorder is mainly due to a lack of connectivity among the V—O polyhedra (thus reducing LRO). Additionally, the RDFs predicted by MTP-based MD at 2000 K after 50 ps simulation time (Figure 2c) is quite similar to AIMD calculations, signifying that MTP captures the disordering of V_2O_5 accurately at 2000 K. Also, upon increasing the supercell size to $2 \times 4 \times 6$ and at 2000 K in our MTP-based MD simulations, we can verify the complete melting (or amorphization) of the V_2O_5 structure, as characterized by the broad shoulder on all types of bonds from ≈6.5 to ≈16 Å (see Figure S5b, Supporting Information).

In the case of MgV_2O_5, since we inserted Mg atoms into the AIMD-generated V_2O_5 structures at various temperatures, our

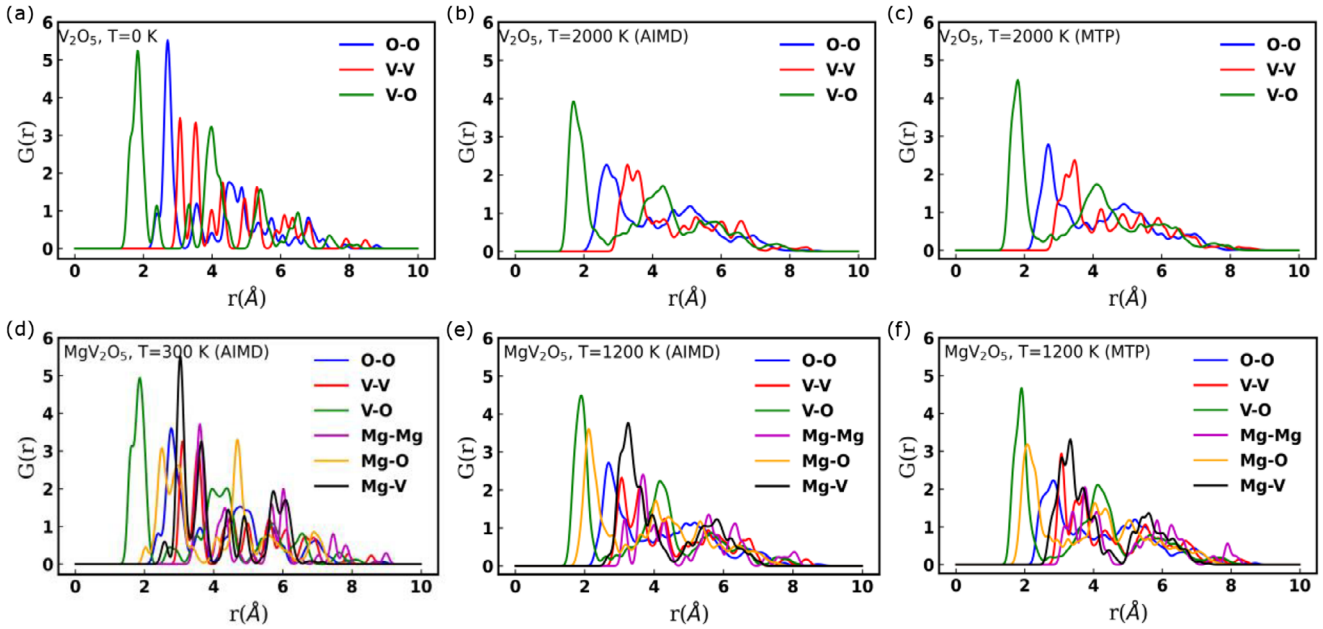

Figure 2. Radial distribution functions (RDFs or $G(r)$) of V_2O_5 (panels a–c) and MgV_2O_5 (panels d–f) calculated using AIMD or MTP under different temperatures. a) Crystalline V_2O_5 (DFT-relaxed at 0 K), b) AIMD-generated V_2O_5 at 2000 K after 4 ps, c) MTP-generated V_2O_5 at 2000 K after 50 ps, d) AIMD-generated MgV_2O_5 at 300 K after 4 ps, e) AIMD-generated MgV_2O_5 at 1200 K after 4 ps, and (e) MTP-generated MgV_2O_5 at 1200 K after 50 ps. Blue, red, green, purple, orange, and black lines signify O—O, V—V, V—O, Mg—Mg, Mg—O, and Mg—V bonds, respectively.

dataset lacks a truly crystalline representation of MgV_2O_5. Thus, the AIMD-generated MgV_2O_5 structure at 300 K, after 4 ps simulation time (Figure 2d) is the closest representation of crystalline MgV_2O_5 in our dataset. The crystalline nature of MgV_2O_5 at 300 K is characterized by its sharp peaks in the pair correlations for all types of bonds, including Mg–O (orange), Mg–V (black), and Mg–Mg (purple), as seen in Figure 2d. Analogous to our observation in V_2O_5, the disorder in MgV_2O_5 increases at higher temperatures, as characterized by weaker peaks and broader shoulders beyond ≈6.5 Å in the AIMD-generated structure at 1200 K (after 4 ps simulation time, Figure 2e). Also, the MTP-generated MgV_2O_5 structure at 1200 K (after 50 ps simulation time, Figure 2f) is quite similar to the AIMD-generated version, with the main differences arising out of Mg-Mg peak intensities at ≈3.5 and 4 Å. Thus, our calculated RDFs indicate that we are able to disorder the V_2O_5 and MgV_2O_5 structure significantly during our AIMD simulations, which is captured equally well by our MTP-based MD.

To quantify the LRO in amorphous MgV_2O_5, at various temperatures, we used the open-source python package PyLRO,[90] which calculates the degree of directional disorder based on deviations in atomic spacings along different crystallographic directions. Specifically, we took structures based on our 1 × 2 × 3 supercell after a MTP-MD simulation time of 20 ps at 300 K, 600, 900, and 1200 K, calculated the extent of LRO along various directions, and plotted them in **Figure 3**. Note that the isosurfaces of Figure 3 are depicted on a 3D Miller sphere, with different directions (and their associated Miller indices) indicated as text notations (along each axis). The maximum/minimum disorder in the structures and the disorder along the *a* [100], *b* [010], and *c* [001] axes for all structures are quantified in Table S2 (Supporting Information). We have also included visualizations of the structures used for calculating LRO in Figure S6 (Supporting Information).

Importantly, we observe an intuitive increase in structural disorder, or a decrease in LRO, with increasing temperature, as quantified by an increase in the calculated maximum and minimum disorder values in V_2O_5. For example, the maximum and minimum disorder are 0.11 and 0.01 at 300 K, 0.12 and 0.02 at 600 K, 0.21 and 0.05 at 900 K, and 0.34 and 0.07 at 1200 K, respectively (see Table S2, Supporting Information; Figure 3). While there is some degree of similarity in the extent of (dis)order in the structures at 300 and 600 K, there is a sharp increase in disorder at 900 K and beyond. At all temperatures, we observe intermediate levels of (dis)order along the [100], [010], and [001] directions, relative to the maximum and minimum values across all directions. This suggests that the primary axes of LRO disruption does not align with the orthogonal, Cartesian basis vectors. Thus, the largest disruptions to the LRO in amorphous V_2O_5 occurs along non-orthogonal directions that are not trivial to visualise.

We observe a clear temperature-dependent anisotropy in the breakdown of LRO. At 300 and 600 K, the maximum distortion lies primarily within the *ab*-plane, while at 900 K, it shifts toward the *bc*-plane. At 1200 K, the maximum distortion returns to the *ab*-plane, though with higher overall disorder (Figure 3). This directional variation in disorder across temperatures indicates that the structural deviations are not isotropic but evolve with temperature, reflecting a complex, temperature-dependent anisotropy in the underlying atomic network. Overall, we observe a progressive decline in the LRO of MTP-generated amorphous MgV_2O_5 with increasing temperature, which indicates the robustness of our melt-quench process and the reliability of our constructed MTP.

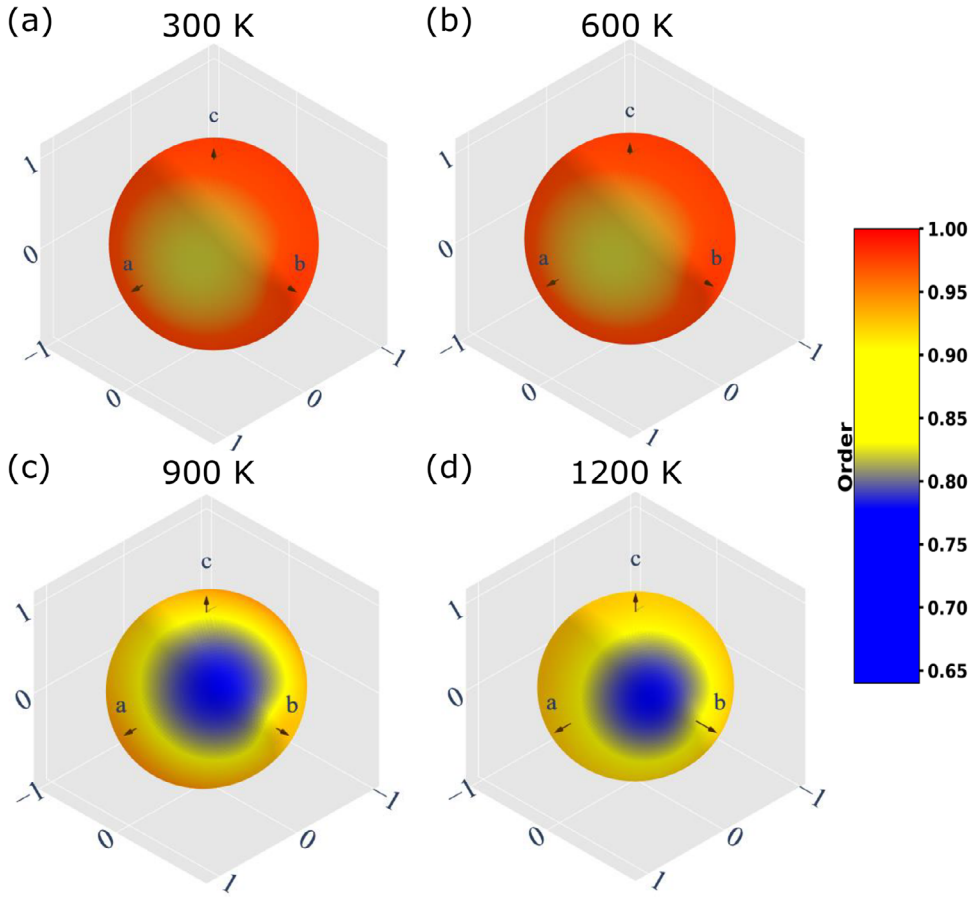

Figure 3. Isosurfaces of calculated LRO, plotted on 3D Miller spheres, in MTP-generated MgV_2O_5 structures at a) 300, b) 600, c) 900, and d) 1200 K, after a simulation time of 20 ps. Cartesian axes of the MgV_2O_5 structure are indicated as text annotations on the spheres. Blue (red) regions of an isosurface indicate low (high) LRO.

3.3. Voltage Predictions

To quantify the impact of amorphization on the voltages of Mg intercalation into V_2O_5, we calculate the average voltages (vs Mg metal) based on AIMD/DFT (blue bars) and MTP (red) structures generated at 600, 900, and 1200 K, and compare the values to the average voltage obtained for the crystalline V_2O_5 structure (denoted as 0 K) in **Figure 4**. For calculating the AIMD voltage in the crystalline structure, we performed a full DFT relaxation of crystalline V_2O_5 and crystalline MgV_2O_5 structures, as available in the ICSD. In the case of MTP, we performed similar structure relaxations of both crystalline structures using LAMMPS. Subsequently, we did a single SCF calculation of the MTP-relaxed structure using the SCAN+U functional. Note that performing the SCF calculations captures the effect of structural disorder that is induced at different temperatures rather than the effect of the temperature itself on the calculated voltages, i.e., the temperatures in Figure 4 are a proxy to indicate the extent of disorder in $(Mg)V_2O_5$ structures used in our voltage calculations.

The SCAN+U calculated voltage for crystalline V_2O_5 (≈2.56 V) is in agreement with the calculated (≈2.52 V) and experimental (≈2.3 V) voltage reported in literature.[22,27] Importantly, the AIMD calculated voltages decrease with increasing disorder in the structure, as indicated by the temperatures at which the structures are generated (see Figure 4). For example, the AIMD average voltage drops to ≈2.3, ≈2.23, and ≈2.19 V at 600, 900, and 1200 K, respectively, reflecting a drop of ≈0.26–0.37 V (10.2–14.4%) compared to the crystalline structure. The drop in average voltage arises from the disruption in LRO which affects the local bonding environment of Mg as it is intercalated into the structure, i.e., the PES at the Mg intercalation sites in the amorphous structure is not as deep as those encountered in the crystalline structure. Note that the more stable the bonding environment of Mg in the discharged state is (i.e., the deeper the PES around a Mg site is) the higher the average intercalation voltage, reflecting the energy gain of putting Mg within a stable environment in the host structure. Thus, a flatter PES, caused by disruption in the LRO of a structure, will naturally result in a lower voltage compared to the corresponding crystalline structure. Such a "flattening" of the PES can indeed enhance Mg diffusion in the amorphous structure (see Section 3.4).

Note that the drop in voltage in amorphous-V_2O_5 is only ≈10–14% compared to crystalline-V_2O_5. Thus, a loss in energy density can be traded-off for a potential gain in Mg diffusivity within the material. For reference, we have included experimental cyclic voltammetry profiles of Mg intercalation in amorphous V_2O_5, as

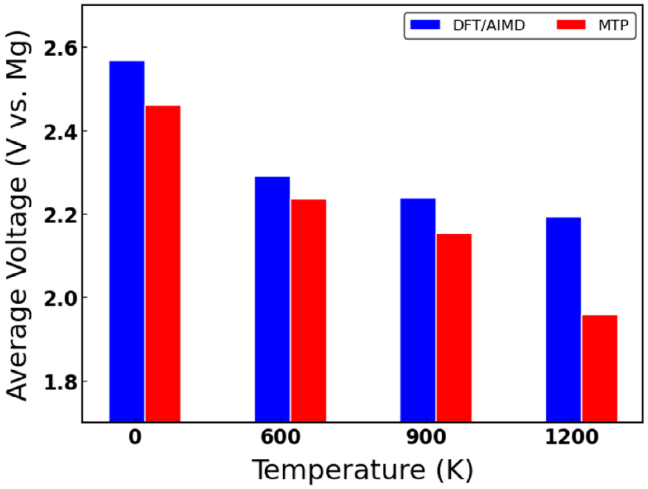

Figure 4. Comparison of average (de)intercalation voltage of Mg in V_2O_5 versus Mg metal, as calculated by AIMD/DFT (blue bars) and MTP (red bars), at different temperatures. 0 K indicates calculations done on the crystalline structure of V_2O_5 and MgV_2O_5.

reported previously,[46] in Figure S15 (Supporting Information). Moreover, the average voltages in amorphous-V_2O_5 are higher than the SOTA chalcogenide Mg cathodes.[20,21,91] Additionally, the MTP-calculated voltage is in fair agreement with the first principles voltages for the crystalline structure (≈2.46 V) as well as the disordered structures, with deviations of ≈0.1 V at 600 and 900 K, indicating that the constructed MTP is able to describe the energetics fairly well. We do observe a significant underestimation in the MTP-based voltage at 1200 K (deviation of ≈0.23 V vs AIMD), which may be due to the specific structure that is sampled for the voltage calculation in the MTP simulation. Nevertheless, trends in our calculated voltages do indicate a possible drop of ≈10% in amorphous V_2O_5 compared to its crystalline version, which needs to be accounted for if the amorphous structure is used as a cathode material in Mg batteries.

3.4. Mg Diffusivities

Figure 5a displays the overall MSD(Δt) as a function of Δt (Equation 4), from MTP-based MD calculations on a $2 \times 4 \times 6$ MgV_2O_5 supercell for 4000 ps. The yellow, blue, green, pink, and red lines in Figure 5a correspond to MSD data at 1200, 1000, 900, 600, and 300 K. We observe linear relationships between MSD and Δt for all temperatures. Note that the MSD displayed in Figure 5a is the overall MSD of Mg-ions, i.e., combining individual displacements along axes *a*, *b*, and *c*. The MSDs along individual axes are shown in Figures S7 and S8 (Supporting Information). The actual MSD(t) data from the MTP calculations as a function of simulation time (t, Equation 2) is shown in Figures S9 and S8 (Supporting Information), which expectedly shows noisier statistics than the MSD(Δt) data. Given the high computational costs associated with AIMD simulations, we only performed AIMD in $1 \times 2 \times 3$ supercell, with the data compiled in Figure S10 (Supporting Information). Data from the corresponding MTP-MD simulations that we ran on a $1 \times 2 \times 3$ supercell over 4000 ps is displayed in Figures S11–S13 (Supporting Information). Our MTP simulations on the larger $2 \times 4 \times 6$ supercell does display less noisy statistics than the data from the smaller $1 \times 2 \times 3$ supercell. The linear relationship between log D (with D in units of $cm^2\ s^{-1}$) and $1/T$, as obtained from the MTP-based MD data on the $2 \times 4 \times 6$ supercell at different temperatures is displayed in Figure 5b, with similar relationships derived from the $1 \times 2 \times 3$ supercell AIMD and MTP data compiled in Figures S10 and S13 (Supporting Information).

Importantly, we estimate the MTP-calculated Mg-diffusivities in amorphous V_2O_5, based on the data in Figure 5a, to be 1.81×10^{-6} $cm^2\ s^{-1}$ at 300 K, 3.41×10^{-6} $cm^2\ s^{-1}$ at 600 K, 4.75×10^{-6} $cm^2\ s^{-1}$ at 900 K, 5.63×10^{-6} $cm^2\ s^{-1}$ at 1000 K, and 8.71×10^{-6} $cm^2\ s^{-1}$ at 1200 K. The associated E_a with this variation of D with T is 47 meV. Such diffusivities and E_a values are a remarkable improvement in Mg mobility in the amorphous V_2O_5 structure compared to the crystalline version. For example, previous studies[17,27,92] have estimated an E_a of 600–750 meV and 975–1120 meV in the δ and α polymorphs of V_2O_5, respectively. The crystalline E_a values correspond to Mg diffusivities in the order of 10^{-13} to 10^{-16} $cm^2\ s^{-1}$ in δ and 10^{-20} to 10^{-22} $cm^2\ s^{-1}$ in α at 300 K. In comparison, amorphous V_2O_5 exhibits a Mg diffusivity in the order of 10^{-6} $cm^2\ s^{-1}$ at 300 K, which is a minimum improvement of ≈7 orders of magnitude in Mg diffusivity compared to the crystalline structure. Given that we have not changed the chemical composition here, this increase in diffusivity is entirely due to the amorphization of V_2O_5, resulting in a flatter PES.

Previously, Mg^{2+} self-diffusivities have been reported to be in the range of 10^{-11} to 10^{-12} $cm^2\ s^{-1}$ at 298 K in the thiospinel $Mg_x Ti_2 S_4$ at $x = 0.35$, with higher diffusivities (≈10^{-8} $cm^2\ s^{-1}$) reported at $x \approx 0$ at 333 K.[8,21] Given that the thiospinel represents one of the SOTA Mg-cathode materials, we expect higher diffusivities in our amorphous oxide, by ≈5 and ≈2 orders of magnitude compared to the thiospinel at 298 and 333 K, respectively. This gain in Mg diffusivity represents a potentially significant gain in power performance. Moreover, amorphous V_2O_5 can yield a higher average voltage (by at least ≈0.8 V) than $Mg_xTi_2S_4$,[21,91] indicating a potential improvement in energy density as well. Thus, improvements in Mg mobility with the disruption of LRO provides a crucial handle that can enable the use of oxide (and other high energy density) cathodes for Mg batteries.

3.5. Degree of Correlation

Figure 6 plots the overall MSCD(Δt) as a function of Δt for amorphous-MgV_2O_5 (panel a) at different temperatures and the variation of H_R with temperature (panel b) based on our MTP-MD calculations on the $2 \times 4 \times 6$ supercell over 4000 ps. Calculated MSCD and H_R data with MTP on the $1 \times 2 \times 3$ supercell is provided in Figure S14 (Supporting Information). Notably, the MSCD's variation with Δt demonstrates non-linearity at high Δt, at intermediate temperatures of 600 and 900 K, which is expected since tracking centre-of-mass displacements can lead to noisier data than tracking individual atoms.[86] Importantly, our calculated H_R shows a strong monotonic dependence of temperature in amorphous-MgV_2O_5, with values increasing from ≈0.46 at 300 K to ≈0.92 at 1200 K. Notably,

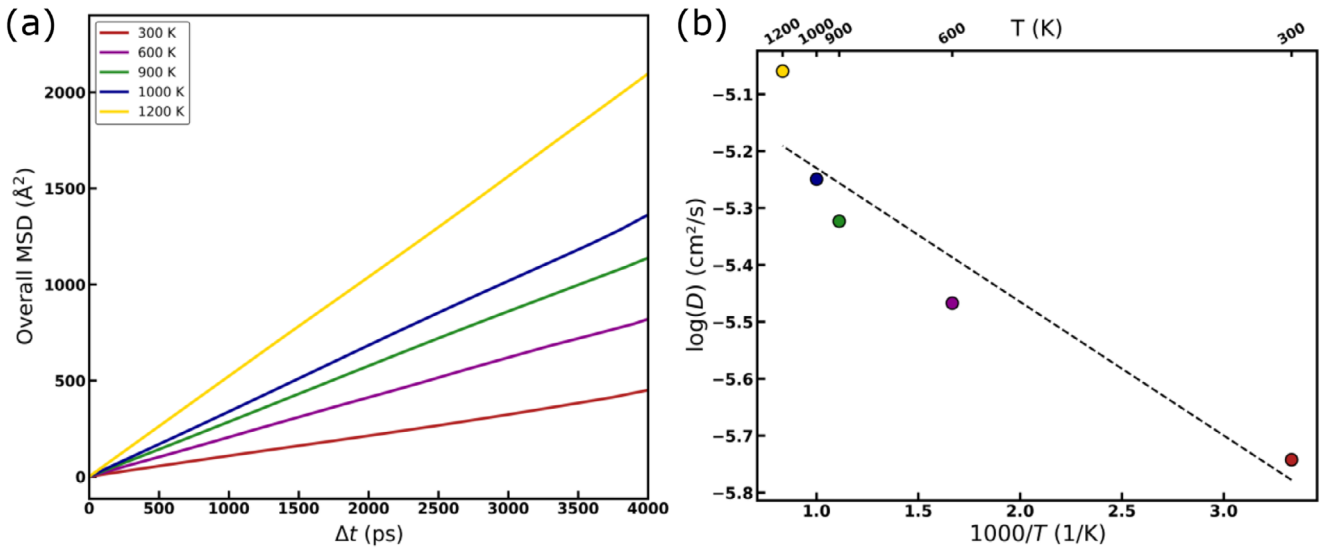

Figure 5. a) Overall MSD(Δt) values as a function of Δt, calculated with MTP-MD over 4000 ps in a $2 \times 4 \times 6$ MgV_2O_5 supercell. Yellow, blue, green, pink, and red lines represent calculated data at 1200, 1000, 900, 600, and 300 K, respectively. b) Arrhenius plot of log D (with D in $cm^2\ s^{-1}$) versus $1000/T$, derived from the data in panel a. Colors of the dots correspond to the temperatures in panel a. Dashed black line represents a linear fit.

diffusion along grain boundaries in metals (i.e., highly defective regions) is also known to be highly correlated, especially at low temperatures,[42] in qualitative agreement with our predictions for an amorphous oxide. At higher temperatures, the large availability of thermal energy ensures that atoms migrate in a more random (non-correlated) manner compared to lower temperatures, where concerted motion (cross-correlation) seems to occur due to stronger electrostatic interactions. Such concerted motion at low temperatures can possibly be characterized using experimental techniques and can provide a handle to further optimize the diffusivity of Mg ions within the amorphous V_2O_5 lattice by facilitating migration channels that allow for concerted Mg motion.

4. Discussion

In this work, we used a combination of AIMD and MLIP-MD simulations to explore amorphous V_2O_5 as a cathode material for Mg batteries, which form an important alternative technology in the space of beyond-Li-ion batteries. Specifically, we used melt-quench AIMD simulations and active learning (Figure 1) to generate ≈3700 configurations of amorphous V_2O_5 and MgV_2O_5 to train accurate MTPs that yielded RMSE (MAE) of 3.16 (2.33) meV $atom^{-1}$ and 0.244 (0.116) eV $Å^{-1}$ on the test set energies and forces, respectively. We verified the amorphous nature of V_2O_5 and MgV_2O_5 structures obtained using both AIMD and MTP-MD, using RDF and LRO calculations (Figures 2 and 3),

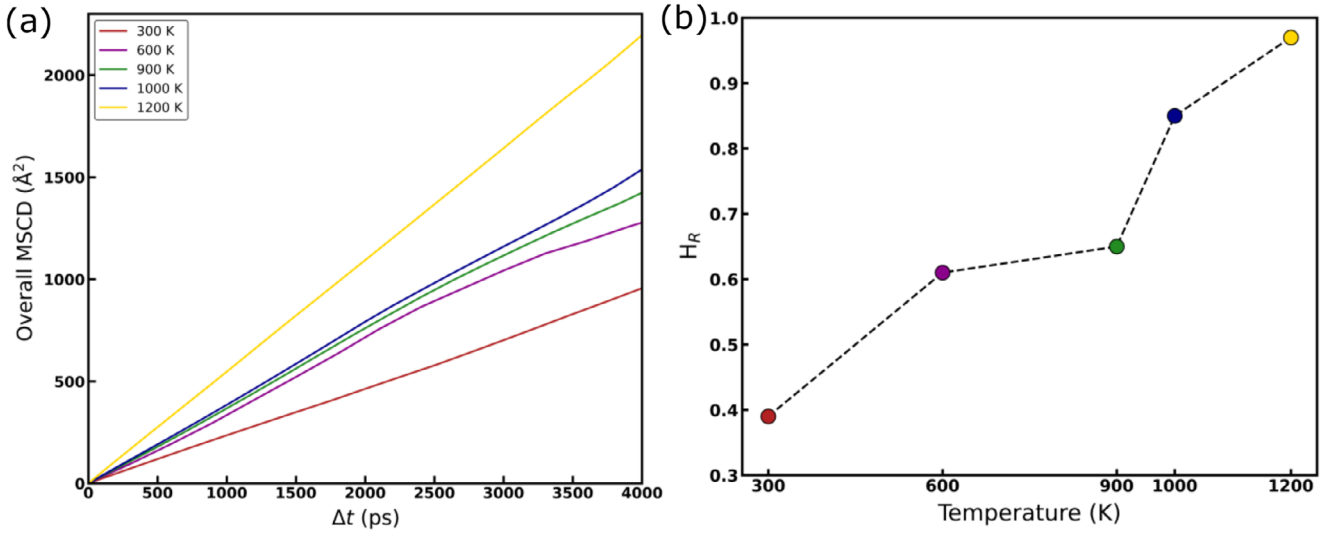

Figure 6. a) Overall MSCD(Δt) as a function of Δt for amorphous MgV_2O_5 at different temperatures, as obtained from MTP-MD simulations in a $2 \times 4 \times 6$ supercell over 4000 ps. b) Variation of calculated H_R with temperature. Yellow, blue, green, pink, and red colors in both panels represent data at 1200, 1000, 900, 600, and 300 K, respectively.

and noted the similarities in the RDFs obtained using AIMD and MTP-MD. Subsequently, we estimated the average Mg intercalation voltages, the Mg diffusivities (and associated E_a), and quantified the extent of cross-correlation in Mg motion, as a function of temperature using MTP-MD performed on large $2 \times 4 \times 6$ supercells over 4 ns. We found that amorphization of V_2O_5 can result in a 10–14% drop in average Mg intercalation voltages compared to crystalline V_2O_5 (Figure 4), depending on the temperature. Importantly, we observed remarkably high Mg diffusivities ($\approx 10^{-6}$ cm^2 s^{-1}, Figure 5) in amorphous MgV_2O_5 at five different temperatures, with a low resultant E_a of ≈47 meV. Our calculated diffusivities in amorphous MgV_2O_5 are ≈7 and ≈5 orders of magnitude higher compared to crystalline $Mg_xV_2O_5$ and thiospinel $Mg_xTi_2S_4$, respectively, highlighting the impact of amorphization on Mg mobility. Also, we found Mg diffusivities to be significantly cross-correlated at low temperatures ($H_R \approx 0.46$ at 300 K, Figure 6) with the Mg motion becoming progressively random at high temperatures ($H_R \approx 0.92$ at 1200 K). Overall, we observe amorphization to be a key handle that can significantly enhance Mg motion in oxides at room temperature, such as V_2O_5, thus enabling the use of high energy density cathodes with reasonable power performance, potentially resulting in the practical deployment of Mg batteries.

Our dataset consists of a total of 3725 configurations comprising V_2O_5 and MgV_2O_5 compositions, generated predominantly using melt-quench AIMD simulations, which was split 90:10 to create the train and test subsets, with our active learning workflow contributing ≈569 configurations for optimizing our MTP. While our dataset is comprehensive and manages to capture the disordering of V_2O_5 quite well (Figure 2), it is limited by the range of temperatures and the lack of intermediate compositions being sampled. Thus, expanding the range of temperatures being sampled (e.g., at every 100 from 300 to 1200 K) and the compositions (e.g., in steps of $\Delta x = 0.1$ in $Mg_xV_2O_5$) will certainly improve the versatility and transferability of our constructed MTPs. Additionally, we used crystalline V_2O_5 (α polymorph) from ICSD as the starting structure for our melt-quench AIMD and added Mg within the amorphized-V_2O_5 structure instead of using MgV_2O_5 (δ polymorph) as a starting configuration, which adds some bias in our dataset. However, given that dataset generation carries the most computational expense in our study, it is impossible for us to encompass all relevant temperatures and compositions and remove all biases for training our MTP. Nevertheless, future works can build upon our dataset by incorporating more diverse data and generating MLIPs with better accuracy and transferability.

We chose MTP for our study for several reasons, including its computational speed using CPU-based processors, ability to learn swiftly from small datasets, and an integrated active learning framework.[57,58,62] Moreover, our previous work has demonstrated that MTP can generalize quite well across multicomponent systems with diverse compositions.[61] Indeed, MTP performs quite well on our AIMD-based dataset, exhibiting low errors on train/test energies and forces, and exhibiting similar RDFs in both amorphous V_2O_5 and MgV_2O_5 structures compared to AIMD (Figure 2; Figures S3–S6, Supporting Information). However, MTP is an invariant potential and does not include features such as equivariance and message passing that is incorporated in more recent graph-based neural network potentials, such as neural equivariance interatomic potential[93] and multi atomic cluster expansion.[94] Thus, MTP is not the most general theoretical framework among MLIPs and does indeed exhibit limited flexibility, accuracy, and transferability.[95] Nevertheless, graph-based potentials are computationally expensive often requiring state-of-the-art GPU-based processors, are demanding on the memory, and are significantly slower on CPUs for MD simulations compared to MTP.[61] In any case, with the expansion of our dataset to more diverse temperatures and compositions, particularly on other oxide based systems, it may be worthwhile to construct graph-based potentials and/or fine-tune some of the available universal MLIPs.[96–99]

One limitation in our voltage predictions, particularly for structures extracted from higher temperatures, is that our voltage calculations have been done on a single snapshot of a structure instead of an average over an ensemble of possible configurations. Note that we don't necessarily expect any qualitative variations or significant quantitative differences between our calculations and ensemble averaged quantities, given that the predicted AIMD/MTP potential energies for both V_2O_5 and MgV_2O_5 (Figure S2, Supporting Information) do not fluctuate significantly at different temperatures. Importantly, we observe a 10–14% drop in the average Mg intercalation voltage in amorphous V_2O_5 compared to its crystalline version (Figure 4), which can result in a 10–14% drop in energy density, a factor that needs to be accounted for in case amorphous V_2O_5 is used as a cathode in Mg batteries. To better understand and quantify the extent of voltage reductions due to amorphization of a given structure, similar studies on other oxides will be useful.

So far, there have been limited experimental studies exploring V_2O_5 (or other oxides) in their amorphous form as cathodes. For instance, Nabavi et al.[45] examined Li-intercalation in amorphous V_2O_5 using using Coulometric titration and reported an open-circuit voltage (OCV) of 3.85–2.0 V, depending on Li content. Similarly, amorphous V_2O_5 has been explored as a cathode in sodium and zinc based batteries, with reports indicating varying electrochemical performance.[100,101] However, experimental studies on Mg with amorphous V_2O_5 are limited. For example, Arthur et al.[102] demonstrated that amorphous V_2O_5–P_2O_5 (75:25 mol%) exhibits improved current density and high-voltage reversibility with an anodic peak at ≈2.9 V versus Mg and a cathodic onset at ≈1.1 V, with the performance improvements attributed to amorphization. Wally et al.[46] demonstrated Mg intercalation on a glass ceramic composite of composition $13.5Na_2S$–$32.5V_2O_5$–$54P_2O_5$ (mol%) that was annealed for 12 h. Specifically, the authors[46] reported an OCV of 1.76 V versus Mg, an initial capacity of 86 mAh g^{-1}, an energy density of 11 Wh kg^{-1}, a coulombic efficiency of 78% after 100 cycles at 55 °C, and voltage plateaus at 1.9 and 2.3 V with significant hysteresis during cycling. Note that the experiments[46] were done on a V_2O_5-P_2O_5 nanocomposite, and possible phase transitions to vanadium phosphates (in addition to amorphization) may have influenced the observed electrochemistry, alongside any electrolyte decomposition, making quantitative comparisons with our computational data difficult. In any case, the reported voltage range of 1.7–2.3 V is within the same range that we expect from our computational results, and we have included the experimentally reported cyclic voltammetry data[46] in Figure S15 (Supporting Information). Nevertheless, more experiments are required to be conducted on amorphous V_2O_5 (and

other oxide systems) to ascertain their suitability as electrode materials.

In terms of diffusivity estimates, sampling more temperatures (and compositions), longer simulations times, and larger supercells, can yield marginally better values than reported in our work (Figure 5). In any case, our MSD(Δt) statistics as calculated by MTP-MD in our $2 \times 4 \times 6$ supercell already appear quite robust (Figures S7–S9, Supporting Information) and provides a good indication of the expected Mg mobility. More importantly, understanding the nature of correlated Mg motion (Figure 6) at lower temperatures will be quite challenging and important to further optimize the performance of amorphous V_2O_5. Specifically, the quenching rate and dopant additions can influence the short range order of amorphous V_2O_5, which in turn can impact the presence of "open channels" for correlated Mg motion. While we provide a visual representation of Mg hops through a compiled video (provided as part of our GitHub repository, see "Data and code availability" section), further characterization using electrochemical impedance spectroscopy, galvanostatic intermittent titration technique, and nuclear magnetic resonance can shed more insights into the underlying migration mechanism(s) that are active. Finally, note that although we report a fairly low E_a (≈47 meV, Figure 5b) for Mg motion in amorphous-MgV_2O_5, the definition of E_a in amorphous systems is not as rigorous as in crystalline systems, since E_a can vary significantly with temperature and the vacancy-based hopping mechanism may not be the only mechanism active in an amorphous structure. Nevertheless, our calculated E_a provides an indication of the swift Mg mobility that is to be expected in amorphous V_2O_5 compared to its crystalline counterpart.

In crystalline solids, ionic diffusion typically occurs via well-defined, vacancy-mediated hopping between regular lattice sites, with a temperature-independent activation barrier determined by the PES. However, in amorphous systems, the lack of a periodic lattice introduces additional complexity in the diffusion mechanism(s). First, the absence of regular lattice sites means that diffusion is strongly influenced by the availability of "free volume" regions of non-bonded space through which ions can migrate, a concept that is well-established in polymeric and glassy systems. We illustrate this using Voronoi tessellation (see videos provided in our GitHub repository as Supporting Information) to show the migration of ions between adjacent polyhedral cages, highlighting the role of free volume and distorted geometrical connectivity in enabling diffusion. Second, at low to moderate temperatures, amorphous V_2O_5 exhibits highly concerted (or correlated) ionic motion, as indicated by the low H_R (Figure 6b), wherein multiple ions migrate simultaneously. This is distinct from individual ionic hopping and can result in a lower effective energy barrier compared to an individual ion hopping across a "static" potential energy landscape, as has been proposed by He et al.[103] During concerted hopping, ions occupying high-energy sites that are stabilized via local Coulomb interactions migrate downhill, which can help reduce the barrier for other ions moving uphill, providing a cooperative effect that facilitates net migration at lower temperatures. Thus, at low to moderate temperatures, both free volume and concerted hopping play a role in the diffusion of Mg in amorphous V_2O_5. As temperature increases, thermal activation enhances ionic mobility and reduces the extent of correlation (as indicated by an increasing H_R, Figure 6b), leading to a more random motion (see supporting videos in our GitHub repository for an illustration).

Our study demonstrates the potential of amorphous oxides, such as V_2O_5, as cathode materials for Mg batteries providing enhanced Mg mobility and a small drop in the intercalation voltage. Moving forward, similar investigations on other amorphous oxide and polyanionic chemistries, whose crystalline versions have shown promise as Li-ion cathodes,[104] such as Mn-, Co-, and Ni-based oxides, and Fe-, and Mn-based phosphates, can be carried out to explore their possible utility as Mg battery cathodes. The workflow established in this study (Figure 1) should provide a theoretical framework for executing studies on analogous cathode chemistries. Moreover, such studies will also provide statistics on the voltage drops, mobility enhancements, and (any) concerted migration mechanisms, which will be useful in improving the fundamental understanding of amorphous systems in general and in guiding the materials design for developing practical Mg batteries.

5. Conclusion

Magnesium batteries offer an alternative technological pathway with potentially higher volumetric energy density, lower costs, and better safety compared to the state-of-the-art LIBs. However, magnesium batteries require cathodes with high energy densities (e.g., oxides) to show reasonable Mg mobility (or power performance) to be practical. In this context, we used MD simulations powered by MLIPs (MTPs) that were trained on systematic melt-quench AIMD data to explore amorphous $Mg_xV_2O_5$ as a cathode for Mg batteries. Upon validating the MTP using active learning and verifying the amorphous nature of the generated structures via RDF and LRO calculations, we performed 4 ns simulations on a $2 \times 4 \times 6$ supercell using MTP-based MD to estimate the Mg intercalation voltage and transport properties. Importantly, we observed a 10–14% drop in the average Mg intercalation voltage and a ≈7 orders of magnitude improvement in Mg diffusivity (with a low E_a of 47 meV) due to amorphization of the V_2O_5 framework. Our predicted Mg diffusivity in amorphous V_2O_5 is higher than in thiospinel $Mg_xTi_2S_4$, by ≈5 orders of magnitude at room temperature. Also, we observed significant cross-correlation in the Mg motion at room temperature, with the motion becoming progressively random at higher temperatures. Thus, we find amorphous V_2O_5 to be a promising cathode material for Mg batteries. More importantly, we expect amorphization of analogous oxides to be a key handle that can be used to design cathodes exhibiting high energy and reasonable power densities for Mg batteries. Finally, our theoretical workflow powered by MLIPs can be extended to explore a broader range of materials and properties, which will be a crucial step in accelerating the design and discovery of new amorphous materials for different applications.

Supporting Information

Supporting Information is available from the Wiley Online Library or from the author.

Acknowledgements

G.S.G. acknowledges financial support from the Indian Institute of Science (IISc) Seed Grant, SG/MHRD/20/0020 and SR/MHRD/20/0013, and

the Science and Engineering Research Board (SERB) of the Department of Science and Technology, Government of India, under sanction numbers SRG/2021/000201 and IPA/2021/000007. V.C. thanks the Institute of Eminence Post-doctoral fellowship awarded by the Indian Institute of Science for financial assistance. D.D. acknowledges the Indian Institute of Science for academic support and the Shell Fellowship for financial support. A portion of the density functional theory calculations showcased in this work were performed with the computational resources provided by the Supercomputer Education and Research Center, Indian Institute of Science. The authors acknowledge National Supercomputing Mission (NSM) for providing computing resources of "PARAM Siddhi-AI," under National PARAM Supercomputing Facility (NPSF), C-DAC, Pune, and supported by the Ministry of Electronics and Information Technology (MeitY) and Department of Science and Technology (DST), Government of India.

Conflict of Interest

The authors declare no conflict of interest.

Author Contributions

V.C. performed all AIMD calculations, constructed MTP, and validated the potential using active learning. D.D. performed MTP-based MD simulations. V.C. wrote the initial draft of the paper. D.D. edited the draft and aided in the visualization of data. G.S.G. supervised all aspects of the work. All authors approve the final version of the manuscript.

Data Availability Statement

The data, scripts, optimised potentials, and video illustrations that support the findings of this study are openly available in GitHub at https://github.com/sai-mat-group/amorphous-MgV2O5, reference number 1.

Keywords

amorphous solid electrodes, machine learned interatomic potentials, Mg batteries, molecular dynamics, V_2O_5

Received: May 14, 2025
Revised: July 8, 2025
Published online:

[1] F. Degen, M. Winter, D. Bendig, J. Tübke, *Nat. Energy* **2023**, *8*, 1284.
[2] M. Fichtner, *Batter. Supercaps* **2022**, *5*, 202100224.
[3] J. Xiao, X. Cao, B. Gridley, W. Golden, Y. Ji, S. Johnson, D. Lu, F. Lin, J. Liu, Y. Liu, Z. Liu, H. N. Ramesh, F. Shi, J. Schrooten, M. J. Sims, S. Sun, Y. Shao, A. Vaisman, J. Yang, M. S. Whittingham, *Chem. Rev.* **2025**, *125*, 6397.
[4] M. Winter, B. Barnett, K. Xu, *Chem. Rev.* **2018**, *118*, 11433.
[5] J. W. Choi, D. Aurbach, *Nat. Rev. Mater.* **2016**, *1*, 16013.
[6] M. S. Whittingham, *Chem. Rev.* **2014**, *114*, 11414.
[7] X. Yu, W. Li, V. Gupta, H. Gao, D. Tran, S. Sarwar, Z. Chen, *Global Challenges* **2022**, *6*, 2200099.
[8] P. Canepa, G. Sai Gautam, D. C. Hannah, R. Malik, M. Liu, K. G. Gallagher, K. A. Persson, G. Ceder, *Chem. Rev.* **2017**, *117*, 4287.
[9] Z. Li, J. Häcker, M. Fichtner, Z. Zhao-Karger, *Adv. Energy Mater.* **2023**, *13*, 2300682.
[10] X. Lei, X. Liang, R. Yang, F. Zhang, C. Wang, C.-S. Lee, Y. Tang, *Small* **2022**, *18*, 2200418.
[11] H. D. Yoo, I. Shterenberg, Y. Gofer, G. Gershinsky, N. Pour, D. Aurbach, *Energy Environ. Sci.* **2013**, *6*, 2265.
[12] R. Shah, V. Mittal, E. Matsil, A. Rosenkranz, *Adv. Mech. Eng.* **2021**, *13*, 16878140211003398.
[13] Y. Zhao, X. Zhang, J. Xiao, H. Fan, J. Zhang, H. Liu, Y. Liu, H. Yuan, S. Fan, Y. Zhang, *ACS Appl. Mater. Interfaces* **2022**, *14*, 6499.
[14] M. Jäckle, A. Groß, *J. Chem. Phys.* **2014**, *141*, 174710.
[15] D. C. Hannah, G. Sai Gautam, P. Canepa, G. Ceder, *Adv. Energy Mater.* **2018**, *8*, 1800379.
[16] G. S. Gautam, X. Sun, V. Duffort, L. F. Nazar, G. Ceder, *J. Mater. Chem. A* **2016**, *4*, 17643.
[17] Z. Rong, R. Malik, P. Canepa, G. Sai Gautam, M. Liu, A. Jain, K. Persson, G. Ceder, *Chem. Mater.* **2015**, *27*, 6016.
[18] R. D. Bayliss, B. Key, G. Sai Gautam, P. Canepa, B. J. Kwon, S. H. Lapidus, F. Dogan, A. A. Adil, A. S. Lipton, P. J. Baker, G. Ceder, J. T. Vaughey, J. Cabana, *Chem. Mater.* **2020**, *32*, 663.
[19] D. Wang, Z. Zhang, Y. Hao, H. Jia, X. Shen, B. Qu, G. Huang, X. Zhou, J. Wang, C. Xu, F. Pan, *Adv. Energy Mater.* **2024**, *34*, 2410406.
[20] D. Aurbach, Z. Lu, A. Schechter, Y. Gofer, H. Gizbar, R. Turgeman, Y. Cohen, M. Moshkovich, E. Levi, *Nature* **2000**, *407*, 724.
[21] X. Sun, P. Bonnick, V. Duffort, M. Liu, Z. Rong, K. A. Persson, G. Ceder, L. F. Nazar, *Energy Environ. Sci.* **2016**, *9*, 2273.
[22] G. Gershinsky, H. D. Yoo, Y. Gofer, D. Aurbach, *Langmuir* **2013**, *29*, 1096.
[23] G. G. Amatucci, F. Badway, A. Singhal, B. Beaudoin, G. Skandan, T. Bowmer, I. Plitz, N. Pereira, T. Chapman, R. Jaworski, *J. Electrochem. Soc.* **2001**, *148*, A940.
[24] P. Novák, R. Imhof, O. Haas, *Electrochim. Acta* **1999**, *45*, 351.
[25] T. D. Gregory, R. J. Hoffman, R. C. Winterton, *J. Electrochem. Soc.* **1990**, *137*, 775.
[26] J. P. Pereira-Ramos, R. Messina, J. Perichon, *J. Electroanal. Chem.* **1987**, *218*, 241.
[27] G. S. Gautam, P. Canepa, A. Abdellahi, A. Urban, R. Malik, G. Ceder, *Chem. Mater.* **2015**, *27*, 3733.
[28] G. S. Gautam, P. Canepa, A. Urban, S. H. Bo, G. Ceder, *Chem. Mater.* **2017**, *29*, 7918.
[29] T. Chen, G. Sai Gautam, W. Huang, G. Ceder, *Chem. Mater.* **2018**, *30*, 153.
[30] B. J. Kwon, K.a-C. Lau, H. Park, Y. A. Wu, K. L. Hawthorne, H. Li, S. Kim, I. L. Bolotin, T. T. Fister, P. Zapol, R. F. Klie, J. Cabana, C. Liao, S. H. Lapidus, B. Key, J. T. Vaughey, *Chem. Mater.* **2020**, *32*, 1162.
[31] B. J. Kwon, L. Yin, H. Park, P. Parajuli, K. Kumar, S. Kim, M. Yang, M. Murphy, P. Zapol, C. Liao, T. T. Fister, R. F. Klie, J. Cabana, J. T. Vaughey, S. H. Lapidus, B. Key, *Chem. Mater.* **2020**, *32*, 6577.
[32] D. C. Hannah, G. Sai Gautam, P. Canepa, Z. Rong, G. Ceder, *Chem. Commun.* **2017**, *53*, 5171.
[33] N. Sa, T. L. Kinnibrugh, H. Wang, G. Sai Gautam, K. W. Chapman, J. T. Vaughey, B. Key, T. T. Fister, J. W. Freeland, D. L. Proffit, P. J. Chupas, G. Ceder, J. G. Bareno, I. D. Bloom, A. K. Burrell, *Chem. Mater.* **2016**, *28*, 2962.
[34] G. S. Gautam, P. Canepa, W. D. Richards, R. Malik, G. Ceder, *Nano Lett.* **2016**, *16*, 2426.
[35] A. Bhadra, S. Swathilakshmi, U. Mittal, N. Sharma, G. Sai Gautam, D. Kundu, *Small Methods* **2024**, *8*, 2400070.
[36] J. A. Blázquez, R. R. Maça, O. Leonet, E. Azaceta, A. Mukherjee, Z. Zhao-Karger, Z. Li, A. Kovalevsky, A. Fernández-Barquín, A. R. Mainar, P. Jankowski, L. Rademacher, S. Dey, S. E. Dutton, C. P. Grey, J. Drews, J. Häcker, T. Danner, A. Latz, D. Sotta, M. R. Palacin, J.-F. Martin, J. M. G. Lastra, M. Fichtner, S. Kundu, A. Kraytsberg, Y. Ein-Eli, M. Noked, D. Aurbach, *Energy Environ. Sci.* **2023**, *16*, 1964.
[37] K. McColl, F. Corà, *J. Mater. Chem. A* **2019**, *7*, 3704.
[38] C. Glaser, M. Sotoudeh, M. Dillenz, K. Sarkar, J. S. Bark, S. Singh, Z. Wei, S. Indris, R. Müller, K. Leopold, L. F. Nazar, A. Groß, J. Janek, *Chem. Mater.* **2025**, *37*, 3353.

[39] P. Canepa, S.-H. Bo, G. Sai Gautam, B. Key, W. D. Richards, T. Shi, Y. Tian, Y. Wang, J. Li, G. Ceder, *Nat. Commun.* **2017**, *8*, 1759.
[40] M. Liu, Z. Rong, R. Malik, P. Canepa, A. Jain, G. Ceder, K. A. Persson, *Energy Environ. Sci.* **2015**, *8*, 964.
[41] C. Kim, P. J. Phillips, B. Key, T. Yi, D. Nordlund, Y.-S. Yu, R. D. Bayliss, S.-D. Han, M. He, Z. Zhang, A. K. Burrell, R. F. Klie, J. Cabana, *Adv. Mater.* **2015**, *27*, 3377.
[42] Y. Mishin, C. Herzig, *Mater. Sci. Eng., A* **1999**, *260*, 55.
[43] M. Nabavi, C. Sanchez, J. Livage, *Philos. Mag. B* **1991**, *63*, 941.
[44] E. Uchaker, Y. Z. Zheng, S. Li, S. L. Candelaria, S. Hu, G. Z. Cao, *J. Mater. Chem. A* **2014**, *2*, 18208.
[45] M. Nabavi, C. Sanchez, F. Taulelle, J. Livage, A. de Guibert, *Solid State Ion.* **1988**, *28–30*, 1183.
[46] N. K. Wally, E. Sheha, B. M. Kamal, A. E. Hannora, M. M. El-Desoky, *J. Alloys Compd.* **2022**, *895*, 162644.
[47] R. Iftimie, P. Minary, M. E. Tuckerman, *Proc. Natl. Acad. Sci. USA* **2005**, *102*, 6654.
[48] Z. Yu, A. Annamareddy, D. Morgan, B. Wang, *J. Chem. Phys.* **2024**, *160*, 054501.
[49] Y. Zuo, C. Chen, X. Li, Z. Deng, Y. Chen, J. Behler, G. Csányi, A. V. Shapeev, A. P. Thompson, M. A. Wood, S. P. Ong, *J. Phys. Chem. A* **2020**, *124*, 731.
[50] V. L. Deringer, M. A. Caro, G. Csányi, *Adv. Mater.* **2019**, *31*, 1902765.
[51] D. M. Anstine, O. Isayev, *J. Phys. Chem. A* **2023**, *127*, 2417.
[52] O. T. Unke, M. Stöhr, S. Ganscha, T. Unterthiner, H. Maennel, S. Kashubin, D. Ahlin, M. Gastegger, L. Medrano Sandonas, J. T. Berryman, A. Tkatchenko, K.-R. Müller, *Sci. Adv.* **2024**, *10*, adn4397.
[53] X. G. Li, C. Hu, C. Chen, Z. Deng, J. Luo, S. P. Ong, *Phys. Rev. B* **2018**, *98*, 094104.
[54] B. Mortazavi, X. Zhuang, T. Rabczuk, A. V. Shapeev, *Mater. Horiz.* **2023**, *10*, 1956.
[55] N. Fedik, B. Nebgen, N. Lubbers, K. Barros, M. Kulichenko, Y. W. Li, R. Zubatyuk, R. Messerly, O. Isayev, S. Tretiak, *J. Chem. Phys.* **2023**, *159*, 110901.
[56] Y. Mishin, *Acta Mater.* **2021**, *214*, 116980.
[57] I. S. Novikov, K. Gubaev, E. V. Podryabinkin, A. V. Shapeev, *Mach. Learn. Sci. Technol.* **2021**, *2*, 025002.
[58] A. V. Shapeev, *Multiscale Model. Simul.* **2016**, *14*, 1153.
[59] C. Wang, K. Aoyagi, P. Wisesa, T. Mueller, *Chem. Mater.* **2020**, *32*, 3741.
[60] J. Wang, A. A. Panchal, G. Sai Gautam, P. Canepa, *J. Mater. Chem. A* **2022**, *10*, 19732.
[61] V. Choyal, N. Sagar, G. S. Gautam, *J. Chem. Theory Comput.* **2024**, *20*, 4844.
[62] E. Podryabinkin, K. Garifullin, A. Shapeev, I. Novikov, *J. Chem. Phys.* **2023**, *159*, 084112.
[63] M. Hellenbrandt, *Crystallogr. Rev.* **2004**, *10*, 17.
[64] J.-X. Shen, J. Varley, *J. Open Source Softw.* **2024**, *9*, 5941.
[65] S. P. Ong, W. D. Richards, A. Jain, G. Hautier, M. Kocher, S. Cholia, D. Gunter, V. L. Chevrier, K. A. Persson, G. Ceder, *Comput. Mater. Sci.* **2013**, *68*, 314.
[66] G. K. Nayak, P. Srinivasan, J. Todt, R. Daniel, P. Nicolini, D. Holec, *Comput. Mater. Sci.* **2024**, *249*, 113629.
[67] M. Aykol, S. S. Dwaraknath, W. Sun, K. A. Persson, *Sci. Adv.* **2018**, *4*, aaq0148.
[68] in *CRC Handbook of Chemistry and Physics*, (Ed: W. M. Haynes), CRC Press, Boca Raton, FL, USA **2014**.
[69] P. P. Ewald, *Ann. Phys.* **1921**, *369*, 253.
[70] Y. Zhu, T. Gao, X. Fan, F. Han, C. Wang, *Acc. Chem. Res.* **2017**, *50*, 1022.
[71] G. G. Amatucci, J. M. Tarascon, L. C. Klein, *J. Electrochem. Soc.* **1996**, *143*, 1114.
[72] G. Kresse, J. Furthmüller, *Comput. Mater. Sci.* **1996**, *6*, 15.
[73] G. Kresse, J. Furthmüller, *Phys. Rev. B* **1996**, *54*, 11169.
[74] G. Kresse, D. Joubert, *Phys. Rev. B* **1999**, *59*, 1758.
[75] G. S. Gautam, E. A. Carter, *Phys. Rev. Mater.* **2018**, *2*, 095401.
[76] O. Y. Long, G. Sai Gautam, E. A. Carter, *Phys. Rev. Mater.* **2020**, *4*, 045401.
[77] J. Sun, A. Ruzsinszky, J. P. Perdew, *Phys. Rev. Lett.* **2015**, *115*, 036402.
[78] S. L. Dudarev, G. A. Botton, S. Y. Savrasov, C. J. Humphreys, A. P. Sutton, *Phys. Rev. B* **1998**, *57*, 1505.
[79] H. J. Monkhorst, J. D. Pack, *Phys. Rev. B* **1976**, *13*, 5188.
[80] A. P. Thompson, H. M. Aktulga, R. Berger, D. S. Bolintineanu, W. M. Brown, P. S. Crozier, P. J. in 't Veld, A. Kohlmeyer, S. G. Moore, T. D. Nguyen, R. Shan, M. J. Stevens, J. Tranchida, C. Trott, S. J. Plimpton, *Comput. Phys. Commun.* **2022**, *271*, 108171.
[81] W. G. Hoover, *Phys. Rev. A.* **1985**, *31*, 1695.
[82] L. Verlet, *Phys. Rev.* **1967**, *159*, 98.
[83] P. K. Hung, L. T. Vinh, D. M. Nghiep, P. N. Nguyen, *J. Phys.: Condens. Matter* **2006**, *18*, 9309.
[84] G. S. Gautam, P. Canepa, in *Magnesium Batteries: Research and Applications*, (Ed: M. Fichtner), Royal Society of Chemistry, London, UK **2020**, pp. 79–113.
[85] M. Aydinol, A. Kohan, G. Ceder, K. Cho, J. Joannopoulos, *Phys. Rev. B Condens. Matter Mater. Phys.* **1997**, *56*, 1354.
[86] X. He, Y. Zhu, A. Epstein, Y. Mo, *npj Comput. Mater.* **2018**, *4*, 18.
[87] A. Fick, *Ann. Phys.* **1855**, *170*, 59.
[88] Y. Mo, S. P. Ong, G. Ceder, *Chem. Mater.* **2012**, *24*, 15.
[89] S. P. Ong, Y. Mo, W. D. Richards, L. Miara, H. S. Lee, G. Ceder, *Energy Environ. Sci.* **2013**, *6*, 148.
[90] K. Parrish, Q. Hu, Q. Zhu, *J. Appl. Phys.* **2025**, *137*, 025101.
[91] X. Sun, P. Bonnick, L. F. Nazar, *ACS Energy Lett.* **2016**, *1*, 297.
[92] G. S. Gautam, P. Canepa, R. Malik, M. Liu, K. Persson, G. Ceder, *Chem. Commun.* **2015**, *51*, 13619.
[93] S. Batzner, A. Musaelian, L. Sun, M. Geiger, J. P. Mailoa, M. Kornbluth, N. Molinari, T. E. Smidt, B. Kozinsky, *Nat. Commun.* **2022**, *13*, 2453.
[94] I. Batatia, S. Batzner, D. P. Kovács, A. Musaelian, G. N. C. Simm, R. Drautz, C. Ortner, B. Kozinsky, G. Csányi, *Nat. Mach. Intell.* **2025**, *7*, 56.
[95] I. Batatia, D. P. Kovács, G. N. C. Simm, C. Ortner, G. Csányi, *Adv. Neural Inf. Process Syst.* **2022**, *35*, 11423.
[96] Y. Park, J. Kim, S. Hwang, S. Han, *J. Chem. Theory Comput.* **2024**, *20*, 4857.
[97] I. Batatia, P. Benner, Y. Chiang, A. M. Elena, D. P. Kovács, J. Riebesell, X. R. Advincula, M. Asta, M. Avaylon, W. J. Baldwin, F. Berger, N. Bernstein, A. Bhowmik, F. Bigi, S. M. Blau, V. Cărare, M. Ceriotti, S. Chong, J. P. Darby, S. De, F. D. Pia, V. L. Deringer, R. Elijošius, Z. El-Machachi, F. Falcioni, E. Fako, A. C. Ferrari, J. L. A. Gardner, M. J. Gawkowski, A. Genreith-Schriever, et al., *ArXiv* **2023**, arxiv: 2401.00096.
[98] C. Chen, S. P. Ong, *Nat. Comput. Sci.* **2022**, *2*, 718.
[99] B. Deng, P. Zhong, K. Jun, J. Riebesell, K. Han, C. J. Bartel, G. Ceder, *Nat. Mach. Intell.* **2023**, *5*, 1031.
[100] S. Liu, Z. Tong, J. Zhao, X. Liu, J. wang, X. Ma, C. Chi, Y.u Yang, X. Liu, Y. Li, *Phys. Chem. Chem. Phys.* **2016**, *18*, 25645.
[101] S. Wu, Y. Ding, L. Hu, X. Zhang, Y. Huang, S. Chen, *Mater. Lett.* **2020**, *277*, 128268.
[102] T. S. Arthur, K. Kato, J. Germain, J. Guo, P.-A. Glans, Y.i-S. Liu, D. Holmes, X. Fan, F. Mizuno, *Chem. Commun.* **2015**, *51*, 15657.
[103] X. He, Y. Zhu, Y. Mo, *Nat. Commun.* **2017**, *8*, 15893.
[104] M. S. Whittingham, *Chem. Rev.* **2004**, *104*, 4271.